Sequential reduction of slope stability uncertainty based on temporal hydraulic measurements via the ensemble Kalman filter

Liu, K.; Vardon, P. J.; Hicks, M. A.

DOI
10.1016/j.compgeo.2017.09.019

Publication date
2018

Document Version
Accepted author manuscript

Published in
Computers and Geotechnics

Sequential reduction of slope stability uncertainty based on temporal hydraulic measurements via the ensemble Kalman filter

Liu, K., Vardon, P. J., Hicks, M. A.

Geo-Engineering Section, Faculty of Civil Engineering and Geosciences, Delft University of Technology, The Netherlands

Abstract: A data assimilation framework, utilising measurements of pore water pressure to sequentially improve the estimation of soil hydraulic parameters and, in turn, the prediction of slope stability, is proposed. Its effectiveness is demonstrated for an idealised numerical example involving the spatial variability of saturated hydraulic conductivity, k_{sat}. It is shown that the estimation of k_{sat} generally improves with more measurement points. The degree of spatial correlation of k_{sat} influences the improvement in the predicted performance, as does the selection of initial input statistics. However, the results are robust with respect to moderate uncertainty in the spatial and point statistics.

Keywords: Data assimilation, ensemble Kalman filter, finite elements, random fields, slope reliability, spatial variability.

1. Introduction

The slope stability of an embankment subjected to cyclic water level fluctuation is crucial in geotechnical engineering (Huang et al. 2014; Polemio and Lollino 2011; Serre et al. 2008), with the distribution of pore water pressure (PWP) under seepage being particularly relevant in any slope stability assessment (Cho 2012; Zhu et al. 2013). To accurately estimate the PWP, a precise determination of the soil hydraulic parameters is required. However, because it is not realistic to conduct in-situ testing everywhere, some uncertainty remains due to the spatial variability of material properties between measurement locations. This causes difficulty in accurately predicting the seepage behaviour and distribution of pore pressures, and, thereby, the embankment stability.

Data assimilation, which can utilise field measurements, is one method of improving the prediction of slope behaviour, because it can improve the estimation of soil parameters. Data assimilation is defined here as any method to include measured data into numerical analyses. Often, a type of data assimilation known as back-analysis is used, where parameters for the analysis are estimated using measured data available at a certain time (normally the end of the period under consideration). Most previous studies related to slope back-analysis have focused on soil shear strength parameters (Gilbert et al. 1998; Ledesma et al. 1996; Zhang et al. 2010), in which the utilised measurements were mainly displacement or stress/strain. PWP measurements are seldom used in geotechnical engineering, although, in hydrology, it has already been proven that such measurements improve the estimation of hydraulic parameters (Zhou et al. 2014). In geotechnical engineering, the improved accuracy of hydraulic parameters not only benefits the estimation of PWP but also the prediction of slope stability (Vardon et al. 2016).

A limited number of studies have investigated the influence of improved estimation of hydraulic parameters on slope stability, although they have usually ignored the spatial variability of parameter values. For example, Zhang et al. (2013) applied the Bayesian method to back-calculate hydraulic parameters by utilising PWP measurements and investigated the effect of uncertainty in the parameters on the prediction of slope stability, but without incorporating spatial variability. In contrast, Vardon et al. (2016) linked the ensemble Kalman filter (EnKF) (Evensen 1994; 2003) with the random finite element method (RFEM) (Griffiths and Fenton 1993) in steady state seepage to back-calculate the hydraulic conductivity based on PWP measurements. They cross-correlated hydraulic conductivity with the strength parameters (cohesion and friction angle) and investigated the influence of the improved estimation of hydraulic conductivity on the distribution of the factor of safety (FOS). Meanwhile, Jafarpour and Tarrahi (2011) indicated that an imprecise knowledge of the spatial continuity could induce erroneous estimations of soil property values, whereas Pasetto et al. (2015) investigated the influence of sensor failure on the estimation of k_{sat}, focusing on two cases with different correlation lengths. The results demonstrated that the identification of k_{sat} was more accurate for the larger correlation length. Hommels et al. (2001) compared the EnKF with the Bayesian method and concluded that the EnKF, essentially a step-wise Bayesian method, was easier to implement, as it does not require the assimilation of all available data and could sequentially improve the estimation of parameters once further data become available.

In this paper, the authors account for the spatial variability of k_{sat}, which plays a dominant role in rainfall infiltration as pointed out by Rahardjo et al. (2007). In addition, the EnKF is applied to improve the estimation of the k_{sat} field by using (in this instance, numerically generated) 'measurements' of PWP. Due to the existence of spatial variability, the spatial correlation length and arrangement and number of measurement points can have an influence on the data assimilation. Therefore, these aspects are also investigated.

The paper is organised as follows. Firstly, the formulations of stochastic transient seepage, the EnKF and slope stability are introduced. Then, a synthetic example is analysed, to demonstrate the sequential reduction of the uncertainty in k_{sat} and the influence on the subsequent prediction of slope stability. Finally, an investigation into the influence of the pointwise statistics and spatial continuity of k_{sat} on the data assimilation process via the EnKF, utilising synthetic data, has been undertaken.

2. Formulation

2.1. Framework of the overall analysis

Vardon et al. (2016) utilised hydraulic measurements in steady-state seepage to reduce slope stability uncertainty via the EnKF. The formulation of the numerical approach was also given. This paper extends the research to transient seepage, as illustrated by the framework shown in Figure 1.

With reference to Figure 1 (a), the analysis starts by generating an initial ensemble of realisations of the spatial variation of k_{sat}, based on the probability distribution and scales of fluctuation of k_{sat} (i.e. multiple random field realisations of k_{sat} are generated). The initial ensemble of k_{sat} is imported into a stochastic transient seepage process. When the time t reaches t_1, the measurements that have been acquired from the field can be used in the data assimilation process; that is, the EnKF is applied to improve the estimation of k_{sat} for all realisations in the ensemble, based on the measured data. The slope reliability can also be calculated, although, as it is the first time the EnKF is used in the transient seepage process, there is no immediate improvement in the estimated pore pressure. The two options are represented by calculation boxes A and B in Figures 1 (b) and 1 (c), respectively. The analysis then continues until the time reaches t_2, whereupon the computation of pore water pressure resulting from the improved estimation of k_{sat} (calculated at t_1) can be used to compute the slope reliability. At the same time the EnKF can again be applied to get an updated estimation of k_{sat}, since new PWP measurement data have been acquired. As the analysis proceeds still further, the data assimilation continues to t_3, t_4 and so on, with calculation box A or B being followed at each stage.

2.2 Slope stability assessment under transient seepage

The governing equation of 2D transient unsaturated–saturated flow is based on mass conservation, as described in Liu et al. (2015; 2017). To solve it, both the soil water retention curve (SWRC), which describes the relationship between the suction head, h_s, and the volumetric water content, θ, and the saturated–unsaturated hydraulic conductivity relationship are necessary. In Liu et al. (2015; 2017), the Van Genuchten–Mualem model (Mualem 1976; Van Genuchten 1980) was used to describe the relationship between h_s and θ, and the impact of hysteresis was examined. Herein, the effect of hysteresis is not taken into account, in order to simplify the computation. The hydraulic conductivity of an unsaturated soil can also be derived using the Van Genuchten (1980) model. Figures 2 (a) and 2 (b) show the volumetric water content and hydraulic conductivity of the unsaturated soil, respectively, as functions of the suction head.

As in Liu et al. (2015; 2017), Bishop's effective stress, incorporating the influence of both suction and water content, has been combined with the extended Mohr−Coulomb failure criterion to calculate the shear strength.

2.3 Soil parameter random fields

The spatial variability of soil parameters is simulated by the generation of random fields, which are based mainly on the statistical distributions and spatial correlations of the parameters. The distribution of a soil parameter is often assumed to be normal or log-normal, and characterised by the mean and standard deviation. In this paper, the distribution of k_{sat} is considered to be log-normal (Griffiths and Fenton 1993; Zhu et al. 2013), so that the natural log of k_{sat}, $\ln k_{sat}$, follows a normal distribution. The spatial correlation of soil parameters is here characterised by the scale of fluctuation (SOF), l, which is the distance over which parameters are significantly correlated and the exponential correlation function. A more detailed description of the SOF and exponential correlation function are given in Fenton and Griffiths (2008).

In this paper, the random fields have been generated using local average subdivision (LAS) (Fenton and Vanmarcke 1990), using the computer module implemented by Hicks and Samy (2002; 2004). After the random fields of soil parameters (in this case k_{sat}) have been generated, the values are imported into the finite element program at the Gauss point level and then used in computing the seepage and/or slope stability behaviour. The combined use of random fields and the finite element method (FEM) is often referred to as the random finite element method (RFEM).

2.4. Ensemble Kalman filter (EnKF)

The ensemble Kalman filter, developed by Evensen (1994; 2003), has been linked with RFEM using the implementation described in Vardon et al. (2016). To avoid repetition an extensive description is not included in this paper, although the following brief summary of the method is included.

During the EnKF step, the possible solution space is explored, guided by the difference between the measurements and simulated values (in this case pore pressure) at the same location (including a random value added to each point to allow for measurement errors), and the Kalman gain is calculated in order to minimise the posterior error. This can be considered a Bayesian step. The Kalman gain incorporates the covariance between the measurements (pore pressure) and parameter values (hydraulic conductivity). The comparison between the measurements and simulated values of pore pressure is only made at the current step, whereas a full Bayesian approach would seek to include all data.

The difference between this paper and Vardon et al. (2016) is that, here, the measurement of PWP is from a transient seepage process, so that the analysis is able to capture additional information as time progresses. Theoretically, the EnKF can be applied at any time that measurements are acquired. However, because it requires a lot of computational effort, the authors have applied the EnKF at selected practical time steps during the transient seepage process.

3. Illustrative analysis

An idealised embankment subjected to cyclic water level fluctuation has been taken as an example to demonstrate the behaviour of the proposed approach; that is, in sequentially improving the estimation of k_{sat} by using PWP measurements and thereby the influence of the updated hydraulic parameters on the prediction of slope stability.

The geometry of the embankment is shown in Figure 3. Its height is 12 m, and the width of the crest and base are 4 m and 52 m, respectively. The embankment experiences a water level fluctuation on the upstream side, with $\mathrm{WL1}$ and $\mathrm{WL2}$ being the highest and lowest water levels. The downstream water level remains at foundation level (z = 0 m). The bottom boundary is impermeable and fixed.

The water level fluctuation has been simulated by the summation of two sinusoidal curves (Figure 4). T_1 = 1000 days is the time period of sinusoidal 1 (component 1 in Figure 4) and T_2 is the time period of sinusoidal 2 (component 2 in Figure 4), in which $T_1 = 3T_2$. The small arrows in the figure indicate the times at which the pore water measurement data were acquired and the EnKF applied, while the numbers along the top of the figure indicate which application of the EnKF the arrows refer to. The slope stability analyses have been done directly before the 2nd, 4th, 6th, 8th, 10th and 12th data assimilation steps. The random error used in the EnKF, representing the measurement uncertainty (see Vardon et al. (2016) for details), was taken from a normal distribution with a mean of zero and a standard deviation of 0.001 m.

In the embankment, the heterogeneity of k_{sat} has been characterised by its probability distribution, i.e. as characterised by the mean, μ, and standard deviation, σ, of k_{sat}, and by the SOF, l. The mean and coefficient of variation of k_{sat} are assumed to be 1.0 × 10^{-8} m/s and 1.0, respectively, whereas the vertical and horizontal SOFs of k_{sat} are assumed to be $l_v = 1.0$ m and $l_h = 8.0$ m, respectively. The mechanical parameters and other hydraulic parameters are assumed to be deterministic and are listed in Table 1. These values are typical for organic soils.

LAS has been used to generate 1000 random fields as initial ensemble members. It has also been used to generate a single reference realisation, based on the same statistics as used for the ensemble. This is to represent 'real' values of hydraulic conductivity (as might be obtained from the field) and has been used in the seepage analysis to produce 'real' data of PWP to be assimilated.

Two indicators are used to evaluate the performance of the EnKF:

$$\mathrm{RMSE} = \sqrt{\frac{1}{N_k}\sum_{i=1}^{N_k}\left(\left(\ln k_{sat}^{i}\right)^{r} - \left(\ln k_{sat}^{i}\right)^{e}\right)^{2}} \tag{1}$$

$$\mathrm{SPREAD} = \sqrt{\frac{1}{N_k}\sum_{i=1}^{N_k}\mathrm{VAR}(i)} \tag{2}$$

where RMSE is the root mean square error and SPREAD is a measure of the uncertainty of the ensemble members, and in which i is the Gauss point number, N_k is the number of unknown k_{sat} values in the embankment, superscripts r and e indicate the 'real' and ensemble mean values, respectively, and $\mathrm{VAR}(i)$ is the ensemble variance for each unknown k_{sat}, computed over all ensemble members.

4. Results

4.1. Example analysis

This section demonstrates the capability of the EnKF in sequentially improving the estimation of the spatially varying k_{sat}, as well as the subsequent prediction of slope stability.

4.1.1. Estimation of k_{sat} via the EnKF

The number of measurement points used in the EnKF is 63, and the locations are shown in Figure 5 and Table 2. Figure 6 shows the comparison between the reference $\ln k_{sat}$ field, and the initial and improved estimations of the same field. It is seen that, after data assimilation, the estimated local variability of k_{sat} is significantly improved.

Figure 7 shows the reduction of the RMSE and ensemble spread of k_{sat}. Whereas the RMSE decreases quickly in the first few assimilation steps and becomes stable thereafter, the SPREAD decreases continuously. Based on Equation (1), the decrease in RMSE indicates that the estimation of k_{sat}, i.e. the ensemble mean of k_{sat}, becomes closer to the 'real' value. Based on Equation (2), the decrease in SPREAD indicates that the variability of k_{sat} at each Gauss point becomes smaller. This implies that the system is more certain that this is the best result it can calculate with the measurements and solution space available. The value to which the RMSE converges depends on the parameter values in the system which affect the result at the measurement locations. If there are parameter values which do not affect the measurements, the covariance of the measurements and parameters used in the Kalman gain is negligible, and therefore they are not adjusted. Moreover, a random error representing the measurement error is added to each measurement in each assimilation step, and the level of this noise also affects the RMSE value.

Figure 8 compares, for each Gauss point in the finite element mesh, the ensemble mean of $\ln k_{sat}$ with the reference $\ln k_{sat}$. The straight diagonal line in the figure indicates a perfect match between the two quantities. Therefore, the closer to the line a circle (representing a Gauss point value) is, the closer the ensemble mean k_{sat} of this point is to the reference k_{sat}. The colour of the circle represents the numbering of the Gauss points, i.e. from 1 to 2784. In addition, the size of the circle indicates the ratio of the horizontal to vertical coordinates of the points, i.e. x/z. Figure 8 shows the ensemble means of $\ln k_{sat}$ getting closer to the reference $\ln k_{sat}$ as the number of assimilation steps increases.

4.1.2. Prediction of slope stability

The improved estimation of k_{sat} results in an improvement in the estimation of PWP. This influences the effective stress, which, in turn, influences the prediction of slope stability. Figure 9 shows the distributions of FOS with and without data assimilation, i.e. the probability density function (PDF) and cumulative distribution function (CDF) at different times, as well as the corresponding improved $\ln k_{sat}$ random fields. The solid vertical line represents the 'real' FOS calculated using the PWP derived from the reference k_{sat} field. It is seen that the prediction of slope stability can be improved via data assimilation using PWP measurements, due to the standard deviation of the FOS decreasing compared to the original distribution. This is mainly due to the decreased ensemble spread of k_{sat} (Figure 7), which reduces the uncertainty in the estimation of PWP and, in turn, the uncertainty in the slope stability. It is seen that the updated results yield a mean which consistently overpredicts the FOS, although the FOS is part of the PDF predicted at all times. This is thought to be due, at least in part, to the selected measurement data and the log-normal distribution of the hydraulic conductivity.

Note that Figure 9 (e) shows the mean of the predicted FOS just before the 10th assimilation step to be less accurate than just before the 8th assimilation step (Figure 9 (d)). This is because the error between the 'real' PWP and computed PWP increases. The error is defined as:

$$\mathrm{Error} = \sqrt{\frac{1}{nn}\sum_{j=1}^{nn}\frac{1}{N}\sum_{i=1}^{N}\left(\mathrm{PWP}_{i,j}^{e} - \mathrm{PWP}_{j}^{r}\right)^2} \tag{3}$$

where nn is the number of element nodes, N is the number of ensemble members, and PWP^e and PWP^r are the computed PWP and 'real' PWP based on the reference hydraulic conductivity field, respectively. Figure 10 shows the variation of Error (in terms of PWP head) with time. It is seen that the Error increases at $t = 5T_2$, causing the mean of the FOS in Figure 9 (e) to move to the right relative to the 'real' solution and the standard deviation of the FOS to increase. The Error increase is due to the increased uncertainty in the PWP, which is due to the transient drying–wetting seepage process. The uncertainty in the PWP changes with time, partly due to the non-linearity of the SWRC and partly because some soils are still drying while others may be wetting. Figures 9 (f), 9 (l) and 9 (r) are the results at $t = 2T_1$, revealing that the mean of the predicted FOS starts getting closer to the reference FOS again.

To further illustrate this, the computation of the seepage process and slope stability have been extended to $8T_2$. Figure 11 (a) shows the variation of the computed mean FOS and reference FOS with time, and Figure 11 (b) shows the variation of the standard deviation of FOS with time, with and without data assimilation. As expected, the standard deviation is significantly smaller when incorporating data assimilation, although it fluctuates with time as the process continues (due to the fluctuating external loading).

4.2 Sensitivity to the number of measurement points

4.2.1. Estimation of k_{sat}

The estimation of the spatial variability of k_{sat} requires PWP sensors to be installed to capture the local variability. In this section, the influence of different numbers of measurement points on the estimation of k_{sat} is investigated. These points are assumed to be located at selected finite element nodes, as shown in Figure 5 (b), in which the numbers indicated below the embankment are the allocated serial numbers of the columns of measurement points. In order to investigate the influence of the number of measurement points, different numbers of measurement points were used by selecting different combinations of columns. The details are given in Table 2.

The input mean and standard deviation of k_{sat} are the same as in the previous section, as are l_v and l_h. Figure 12 shows the influence of the number of measurement points on the estimation of k_{sat}. It is seen that the RMSE and SPREAD decrease with increasing number of measurement points, albeit with less of an impact on the RMSE above 63 points.

4.2.2. Estimation of slope stability

The influence of the number of measurement points on the prediction of slope stability is shown in Figure 13. It can be seen that, counter-intuitively, the uncertainty in the FOS for 63 measurement points is slightly less than that for 103 measurement points. This is because the uncertainty in the FOS is also influenced by the measurement locations. To illustrate this, Figure 14 shows a comparison between two different configurations of 63 measurement points: the original configuration defined in Table 2, and a second in which the 63 points are located in Columns 0, ±3 and ±12. The uncertainty in the FOS for the second configuration is greater due to the different spatial distribution of measurements throughout the embankment.

4.3 Influence of spatial continuity on the data assimilation

The spatial continuity has been proven to be influential on the estimation of k_{sat} when the EnKF is applied in the data assimilation process (Chen and Zhang 2006; Jafarpour and Tarrahi 2011; Pasetto et al. 2015). When the SOF is large, the local k_{sat} is more likely to be correlated over a relatively long distance. Therefore, it is hypothesised that, for the same number of measurement points, when the SOF (l) is larger, the assimilated results should give a better estimation of k_{sat}. This has been investigated for both isotropic and anisotropic random fields.

4.3.1 Isotropic fields

For isotropic random fields, l_v is equal to l_h. Three different values have been studied here, i.e. l_v = l_h = 2, 8, 64 m, as illustrated by typical random fields shown in Figures 15 (a), 16 (a) and 17 (a), respectively. It is seen that, with an increase in the SOF, the domain becomes nearer to a homogeneous field.

Figure 18 shows that the RMSE and SPREAD for the three SOFs decrease with an increase in the number of assimilation steps. Moreover, when the SOF is larger, the RMSE is smaller which indicates that the updated estimation of k_{sat} is more accurate. The SPREAD is also less for a larger SOF. Figures 15–17 compare the reference and updated $\ln k_{sat}$ fields for different values of l.

Figure 19 shows that the original standard deviation of the FOS increases with an increase in SOF. When the EnKF is applied, by comparing the original and updated standard deviations, it is seen that the reduction of the standard deviation of the FOS is greatest for the largest SOF.

4.3.2 Anisotropic fields

In practice, due to the depositional process of soil, the horizontal SOF tends to be larger than the vertical SOF. In this section, the vertical SOF is assumed to be constant, i.e. $l_v = 1$ m, and the horizontal SOF is l_h = 2, 8, 64 m. The larger l_h leads to horizontal passages of lower resistance to water flow. Figures 6 (a), 20 (a) and 21 (a) show typical random fields for the three horizontal SOFs.

In Figure 22, the number of measurement points is 63, except for l_h = 2 m when two different numbers of measurement points are compared, i.e. 63 and 103. It was found that, when l_h = 2 m, the RMSE does not decrease monotonically when 63 measurement points are used. Since the horizontal SOF is small, indicating that the soil property values are correlated over a small distance, more measurement points have also been considered for this case. Figure 22 shows that the RMSE decreases when 103 measurement points are used. For l_h = 8 m and 64 m, the RMSE decreases with increasing number of assimilation steps. The SPREAD decreases with the number of assimilation steps and the extent of the reduction increases with an increase in l_h (and with an increase in the number of measurement points).

Figures 20 and 21 compare the reference and updated $\ln k_{sat}$ fields for l_h = 2 m and 64 m, respectively. The case with l_h = 8 m is shown in Figure 6.

In Figure 23, when the EnKF is not applied, there is no significant difference in the standard deviations of the FOS. However, when the EnKF is applied, it is seen that the reduction in the standard deviation of the FOS is significant and is highest for l_h = 8 m. This indicates that the reduction of the uncertainty does not simply increase with an increase in the horizontal SOF.

4.4 Influence of initial ensemble statistics

So far, the generated ensembles have been based on the same spatial statistics as used to generate the 'real' field. This section investigates the impact (on the analysis) of generating ensembles from inaccurate input statistics.

4.4.1 Influence of inaccurate SOF

In the previous analyses, the SOF of k_{sat} was used to generate the initial ensemble members via LAS. Chen and Zhang (2006) briefly analysed the influence of an inaccurate integral scale (similar to the SOF) and found that a small deviation (i.e. of 20%) in its value had no significant impact on the assimilation results. However, they also pointed out that wrong information on the statistical anisotropy could have a long-lasting effect on the updated $\ln k_{sat}$ field and that the effect is difficult to eliminate. Therefore, this section analyses a few cases in which l_h is assumed to deviate from the 'real' value, i.e. 50% smaller, 50% larger and 100% larger. In addition, a limiting case where the SOF is assumed to be infinity has been analysed, so that the generated initial ensemble members are based only on the probability distribution of k_{sat}, i.e. on the mean and standard deviation.

Figure 24 shows the comparison of the RMSE and SPREAD between the cases, whereas Figure 25 shows the reference and updated $\ln k_{sat}$ fields corresponding to the 11th assimilation step, which can be compared with the updated field based on the correct SOF of l_h = 8 m in Figure 6 (d). Figure 25 (b) shows that no spatial variability is modelled in the updated $\ln k_{sat}$ field when the starting SOF is infinity. Moreover, Figure 24 shows that the SPREAD with no spatial variability decreases to zero, which implies that the updated estimation of k_{sat} does indeed converge to a single value. Therefore, it can be concluded that the EnKF cannot determine the local variability of k_{sat} without the input of spatial variability in the ensemble members. This can be explained by the calculation of the Kalman gain (Vardon et al., 2016). If no spatial correlation is initially considered, i.e. the field is homogeneous, in each state vector the corresponding values of hydraulic conductivity will be the same (because k_{sat} is the same throughout the mesh). Then the Kalman gain gives a uniform change in the update of k_{sat}, since there is only a single property value in each ensemble member. Therefore, the Kalman gain results in the same updates for all local k_{sat} for each ensemble member, so that the algorithm is not able to search for local variability of k_{sat} in the reference field.

Significantly, Figures 25 (c), 25 (d) and 25 (e) indicate that, when the input horizontal SOF deviates by -50%, +50% and +100% from that of the reference field, the updated estimation of k_{sat} is still acceptable and is almost identical to that obtained when an accurate horizontal SOF is used (Figure 6 (d)).

4.4.2 Influence of inaccurate mean and standard deviation

The influence of the initial mean and standard deviation of k_{sat} has also been investigated, as the initial bias has an influence on the updated estimation of k_{sat} (Dee and Da Silva, 1998). First, only the value of the mean was changed. Then, the values of both the mean and standard deviation were changed. Table 3 lists the inaccurate values used in the data assimilation process. In both cases, accurate SOFs were used.

Figures 26 and 27 compare results between using accurate and inaccurate initial conditions. It is seen that, if only the mean value is inaccurate, there is a big error in the updated estimation of k_{sat} (see Figure 27 (b)). This may be explained by Figure 28, which shows the three input distributions of k_{sat} with different means and standard deviations. It is seen that, when the mean is inaccurate and the standard deviation is relatively small, there is almost no overlap between the area under the solid line (representing the correct distribution) and the dash−dotted line (representing the inaccurate distribution). The results indicate that, when the initial mean is uncertain, it is better to choose a larger standard deviation in order to get acceptable back-calculated results. This is because, if the initial estimation of the mean and standard deviation is inaccurate, choosing a larger standard deviation for generating the initial ensemble enables the realisations to cover a larger range of values, which, in turn, helps in searching out the correct values of k_{sat} during the data assimilation process. Note that, in Figure 28, the distribution curve of k_{sat} based on accurate statistics almost overlaps with the distribution curves of k_{sat} taken from the reference field (Figure 27 (a)) and the estimated field (Figure 27 (c)).

5. Comparison between static and temporal measurements

This section considers the difference between using static measurements from steady-state seepage and temporal measurements from a transient seepage process. For the static measurements, the water level is assumed to be constant at $\mathrm{WL1}$ and the PWP measurements are used to iteratively update the estimation of k_{sat}.

Figure 29 shows the variation of RMSE and SPREAD for the cases using temporal and static PWP measurements, while Figure 30 shows the updated estimation of the $\ln k_{sat}$ field for the two cases. The two figures demonstrate the improvement is better when using temporal measurements, due to more information being available for tuning the results.

6. Conclusions

It has been shown that the measurement of PWP can contribute to an improved estimation of k_{sat}. In the transient seepage process, once the measurement of PWP is acquired, the EnKF can be used to improve the estimation of k_{sat} and, thereby, the estimation of seepage behaviour and slope stability. Significantly, the temporal analysis gives more information for tuning results than a steady-state analysis as implemented in Vardon et al. (2016). It has been found that the precision of the estimation of k_{sat} increases with an increasing number of measurement points, although the uncertainty reduction in the FOS does not monotonically increase with the increasing number. However, it should be noted that, whatever the number of measurement points, the uncertainty in the slope stability can be reduced to a certain extent.

It has also been found that the spatial continuity of k_{sat}, as reflected by the magnitude of the SOF used in random field simulations, has an influence on the estimation of k_{sat} and thereby on the estimation of slope stability. The RMSE of k_{sat} is smaller for a larger l for the same number of measurement points. In addition, the SPREAD of k_{sat} reduces as l gets larger. These results indicate that, when the soil parameters are correlated over a longer distance, the improvement in the estimation of k_{sat}, when using the EnKF based on the same number of measurement points, is greater. For slope stability and isotropic spatial variability, the reduction of the uncertainty in the FOS increases with an increasing l. However, for anisotropic spatial variability (for l_v constant and relatively small compared to the height of the embankment), the reduction of the uncertainty in the FOS does not simply increase with an increasing degree of anisotropy, i.e. l_h/l_v, for the analyses presented in this paper. In addition, although the original standard deviation of the FOS is almost the same for the three values of l_h considered, the updated standard deviation of the FOS shows significant differences for the different l_h.

Last but not least, the initial ensemble statistics of k_{sat} have been investigated. It was found that the EnKF cannot work out the local variability of k_{sat} based only on the measurement data; that is, without considering the spatial variability in the input ensemble. However, even a relatively inaccurate estimation of the SOF, as input for the initial ensemble, can give an updated estimation of k_{sat} that is almost identical to that obtained using the correct SOF. In addition, when the pointwise variation of k_{sat} is not captured well, it is better to assume a larger standard deviation for k_{sat}. This is so that the initial ensemble covers a greater range of values, which helps when searching the parameter space during the assimilation process.

The paper has only utilised synthetic data to validate the proposed framework, so further work is needed to apply this method to a real project with real measurements.

Acknowledgement

The authors would like to thank the China Scholarship Council (CSC), Marie Curie Career Integration Grant (Number 333177) and Geo-Engineering Section of Delft University of Technology, for financial support.

Notation

c'	effective cohesion
e	ensemble mean of k_{sat}
E	stiffness
FOS	factor of safety
G_s	specific gravity of the soil particles
h_s	suction head
$h_{s,ae}$	air-entry suction head
i	Gauss point number
k_{sat}	saturated hydraulic conductivity
l	scale of fluctuation
l_h	scale of fluctuation in the horizontal direction
l_v	scale of fluctuation in the vertical direction
$\ln k_{sat}$	natural log of k_{sat}
n	fitting parameter of the soil water retention curve

N	total number of ensemble members
N_k	number of the unknown k_{sat}
nn	number of element nodes
PWP	pore water pressure
r	'real' value of k_{sat}
RMSE	root mean square error
SOF	scale of fluctuation
SPREAD	uncertainty of the ensemble members
SWRC	soil water retention curve
t	time
T_1	period of the first sinusoid
T_2	period of the second sinusoid
$\mathrm{VAR}(i)$	ensemble variance for each $\ln k_{sat}$
WL	water level
x	coordinate in the horizontal direction
z	coordinate in the vertical direction
α_d	approximately the inverse of the air-entry suction head for soil water retention curve
θ	volumetric water content
θ_s	saturated volumetric water content
θ_r	residual volumetric water content
μ	mean

σ standard deviation

υ Poisson's ratio

ψ Dilation angle

φ' effective friction angle

References

Chen, Y. and Zhang, D. (2006). Data assimilation for transient flow in geologic formations via ensemble Kalman filter. *Advances in Water Resources*, 29(8), 1107-1122.

Cho, S. E. (2012). Probabilistic analysis of seepage that considers the spatial variability of permeability for an embankment on soil foundation. *Engineering Geology*, 133, 30-39.

Dee, D. P. and Da Silva, A. M. (1998). Data assimilation in the presence of forecast bias. *Quarterly Journal of the Royal Meteorological Society*, 124(545), 269-295.

Evensen, G. (1994). Sequential data assimilation with a nonlinear quasi-geostrophic model using Monte Carlo methods to forecast error statistics. *Journal of Geophysical Research: Oceans (1978–2012)*, 99(C5), 10143-10162.

Evensen, G. (2003). The ensemble Kalman filter: Theoretical formulation and practical implementation. *Ocean Dynamics*, 53(4), 343-367.

Fenton, G. A. and Griffiths, D. V. (2008). *Risk assessment in geotechnical engineering*. John Wiley & Sons.

Fenton, G. A. and Vanmarcke, E. H. (1990). Simulation of random fields via local average subdivision. *Journal of Engineering Mechanics*, 116(8), 1733-1749.

Gilbert, R. B., Wright, S. G., and Liedtke, E. (1998). Uncertainty in back analysis of slopes: Kettleman Hills case history. *Journal of Geotechnical and Geoenvironmental Engineering*, 124(12), 1167-1176.

Griffiths, D. V. and Fenton, G. A. (1993). Seepage beneath water retaining structures founded on spatially random soil. *Géotechnique*, 43(4), 577-587.

Hicks, M. A. and Samy, K. (2002). Influence of heterogeneity on undrained clay slope stability. *Quarterly Journal of Engineering Geology and Hydrogeology*, 35(1), 41-49.

Hicks, M. A. and Samy, K. (2004). Stochastic evaluation of heterogeneous slope stability. *Italian Geotechnical Journal*, 38(2), 54-66.

Hommels, A., Molenkamp, F., Heemink, A., and Nguyen, B. (2001). *Effectiveness of inverse modelling techniques applied in geomechanics.* Delft Cluster Publication.

Huang, W.-C., Weng, M.-C., and Chen, R.-K. (2014). Levee failure mechanisms during the extreme rainfall event: a case study in Southern Taiwan. *Natural Hazards*, 70(2), 1287-1307.

Jafarpour, B. and Tarrahi, M. (2011). Assessing the performance of the ensemble Kalman filter for subsurface flow data integration under variogram uncertainty. *Water Resources Research*, 47(5), W05537.

Ledesma, A., Gens, A., and Alonso, E. (1996). Estimation of parameters in geotechnical backanalysis—I. Maximum likelihood approach. *Computers and Geotechnics*, 18(1), 1-27.

Liu, K., Vardon, P. J., Arnold, P., and Hicks, M. A. (2015). Effect of hysteresis on the stability of an embankment under transient seepage. *IOP Conference Series: Earth and Environmental Science, 26 (1), International Symposium on Geohazards and Geomechanics (ISGG2015),* 012013.

Liu, K., Vardon, P. J., Hicks, M. A. and Arnold, P. (2017). Combined effect of hysteresis and heterogeneity on the stability of an embankment under transient seepage. *Engineering*

Geology, 219, 140-150.

Mualem, Y. (1976). A new model for predicting the hydraulic conductivity of unsaturated porous media. *Water Resources Research*, 12(3), 513-522.

Pasetto, D., Niu, G.-Y., Pangle, L., Paniconi, C., Putti, M., and Troch, P. (2015). Impact of sensor failure on the observability of flow dynamics at the Biosphere 2 LEO hillslopes. *Advances in Water Resources*, 86(B), 327-339.

Polemio, M., and Lollino, P. (2011). Failure of infrastructure embankments induced by flooding and seepage: a neglected source of hazard. *Natural Hazards and Earth System Science*, 11(12), 3383-3396.

Rahardjo, H., Ong, T., Rezaur, R., and Leong, E. C. (2007). Factors controlling instability of homogeneous soil slopes under rainfall. *Journal of Geotechnical and Geoenvironmental Engineering*, 133(12), 1532-1543.

Serre, D., Peyras, L., Tourment, R., and Diab, Y. (2008). Levee performance assessment methods integrated in a GIS to support planning maintenance actions. *Journal of Infrastructure Systems*, 14(3), 201-213.

Van Genuchten, M. T. (1980). A closed-form equation for predicting the hydraulic conductivity of unsaturated soils. *Soil Science Society of America Journal*, 44(5), 892-898.

Vardon, P. J., Liu, K., and Hicks, M. A. (2016). Reduction of slope stability uncertainty based on hydraulic measurement via inverse analysis. *Georisk: Assessment and Management of Risk for Engineered Systems and Geohazards*, 10(3), 223-240.

Zhang, L. L., Zhang, J., Zhang, L. M., and Tang, W. H. (2010). Back analysis of slope failure with Markov chain Monte Carlo simulation. *Computers and Geotechnics*, 37(7), 905-912.

Zhang, L. L., Zuo, Z. B., Ye, G. L., Jeng, D. S., and Wang, J. H. (2013). Probabilistic parameter estimation and predictive uncertainty based on field measurements for unsaturated soil slope. *Computers and Geotechnics*, 48, 72-81.

Zhou, H. Y., Gómez-Hernández, J. J., and Li, L. P. (2014). Inverse methods in hydrogeology: evolution and recent trends. *Advances in Water Resources*, 63, 22-37.

Zhu, H., Zhang, L. M., Zhang, L. L., and Zhou, C. B. (2013). Two-dimensional probabilistic infiltration analysis with a spatially varying permeability function. *Computers and Geotechnics*, 48, 249-259.

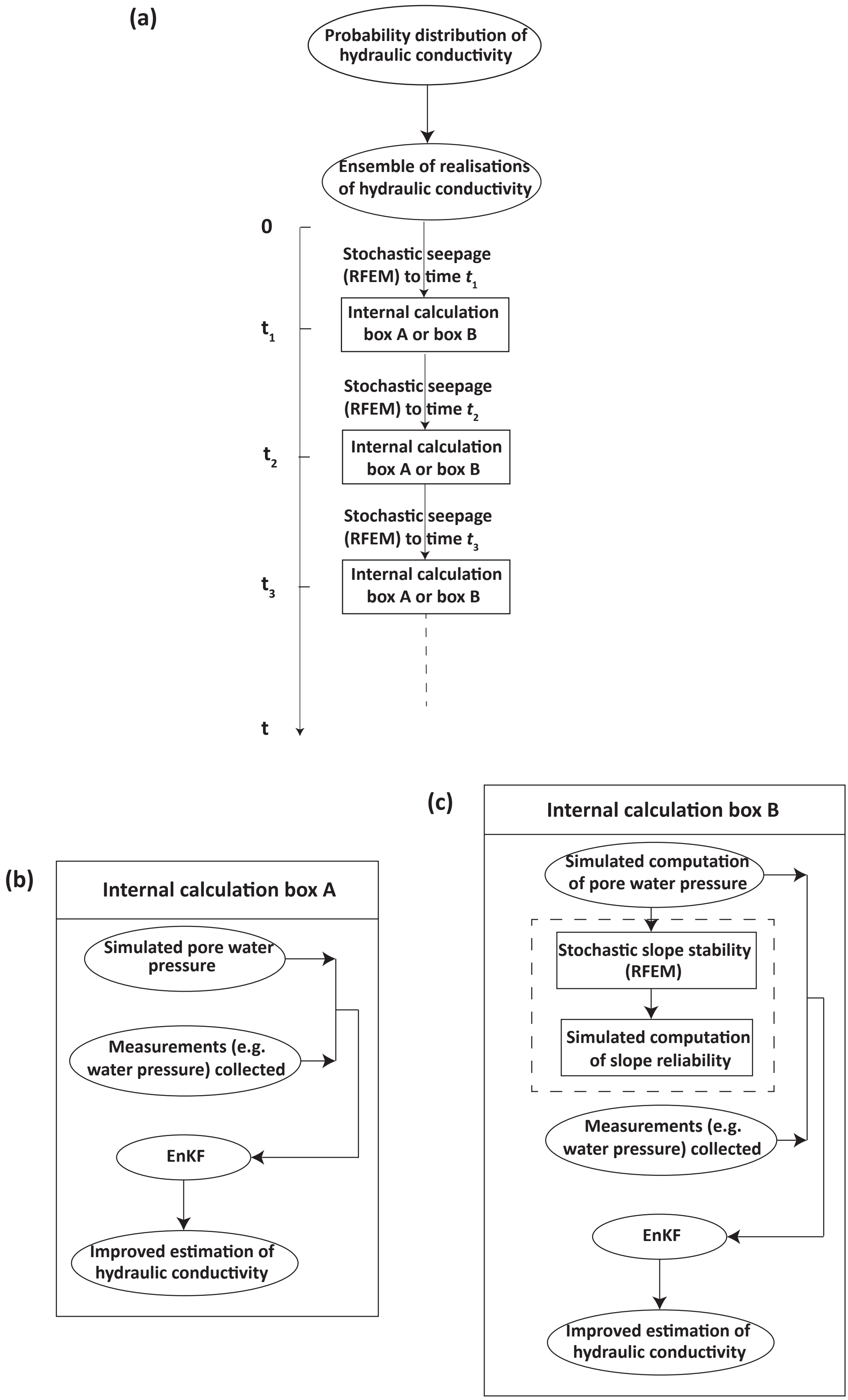

Figure 1 Framework of the numerical approach incorporating transient seepage: (a) Overall flow chart; (b) Details of calculation box A; (c) Details of calculation box B.

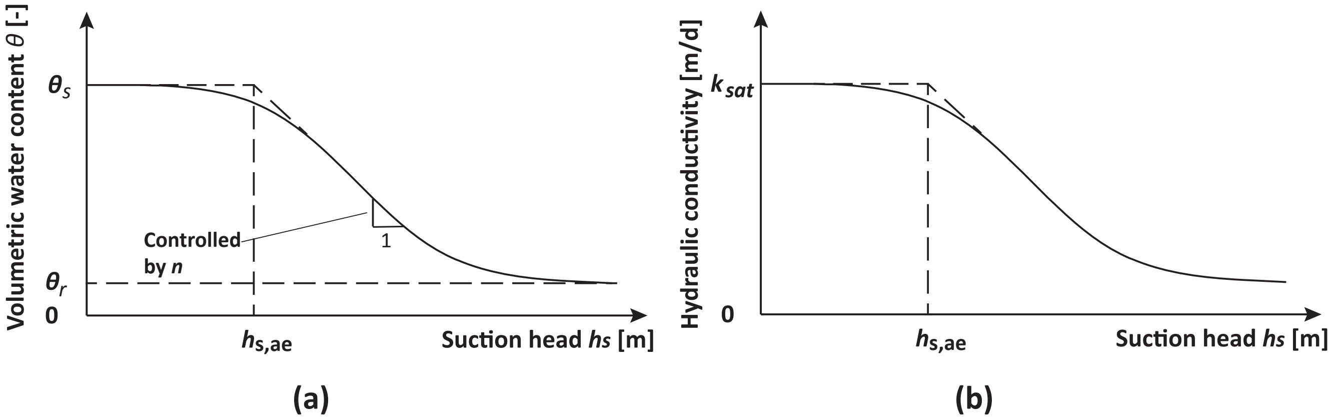

Figure 2 The relationships between suction head and (a) volumetric water content and (b) hydraulic conductivity.

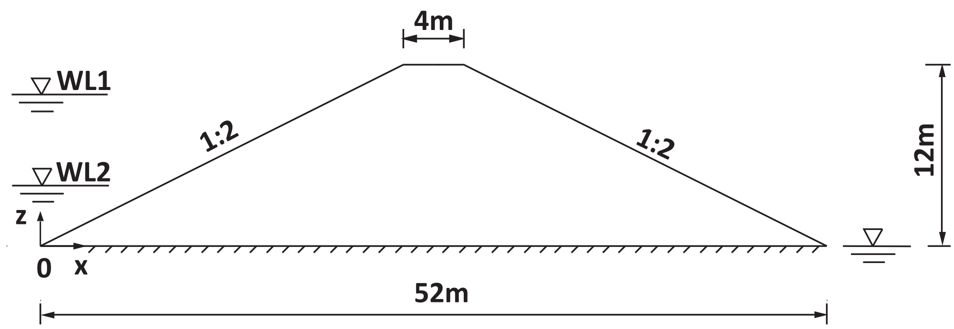

Figure 3 Geometry of the embankment.

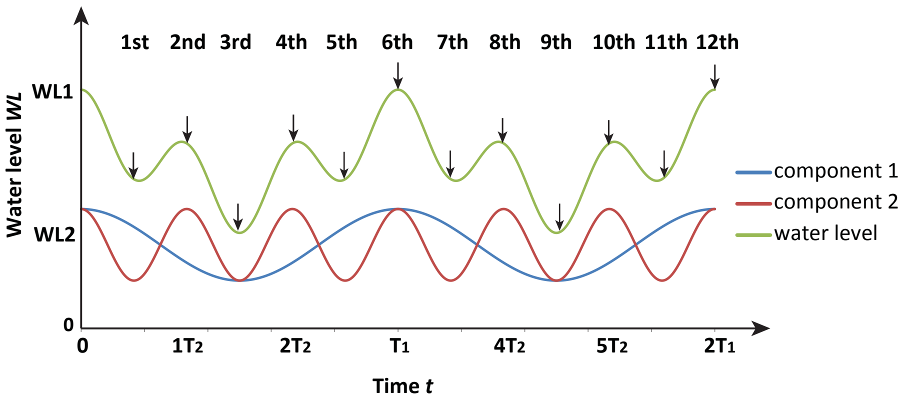

Figure 4 Water level fluctuation simulated by two sinusoidal curves.

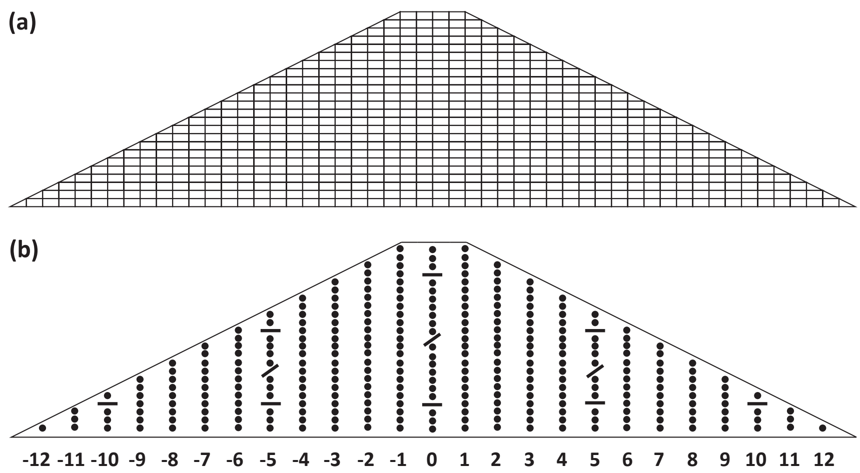

Figure 5 Finite element mesh (a) and location of measurement points (b).

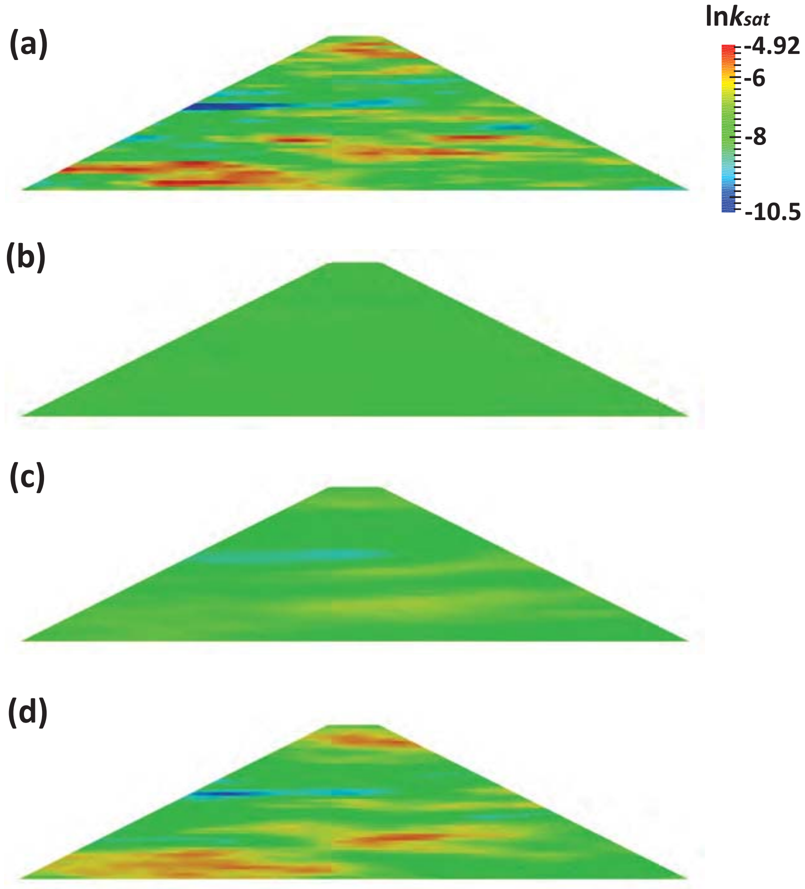

Figure 6 Improved estimation of lnk_{sat} field (l_v = 1 m and l_h = 8 m): (a) Reference field; (b) Initial estimation before assimilation; (c) Improved estimation after 1st assimilation step; (d) Improved estimation after 11th assimilation step.

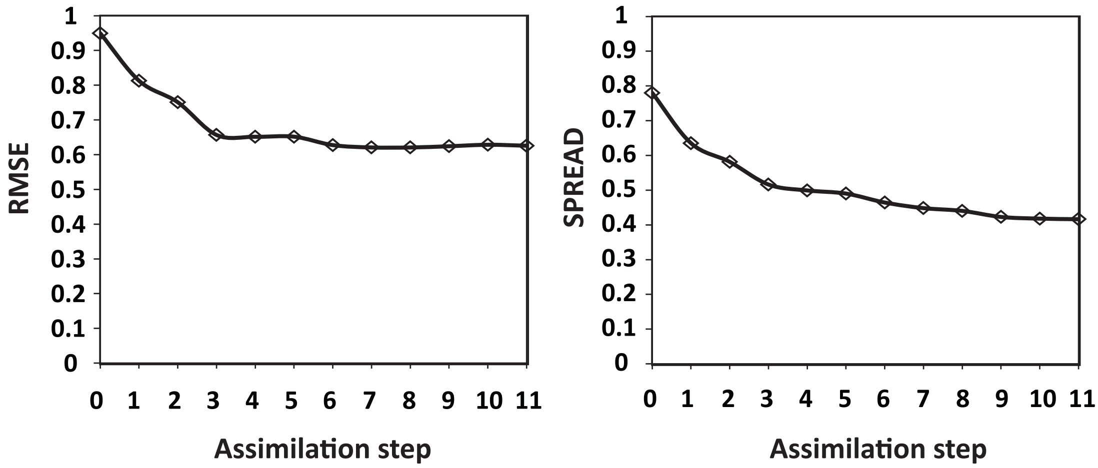

Figure 7 RMSE and SPREAD of k_{sat} as a function of the data assimilation step.

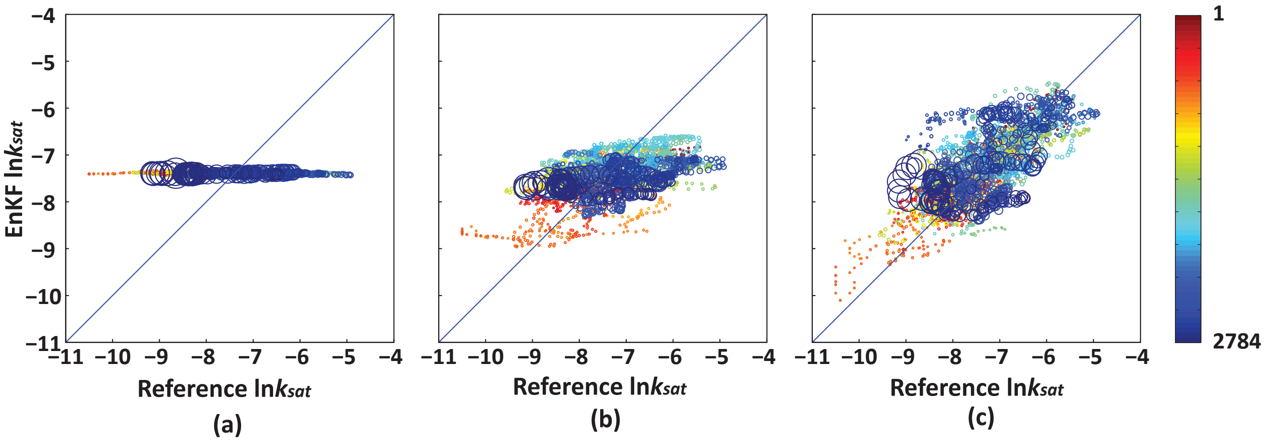

Figure 8 Ensemble mean lnk_{sat} versus reference lnk_{sat}: (a) before data assimilation; (b) after 1st data assimilation step; and (c) after 11th data assimilation step.

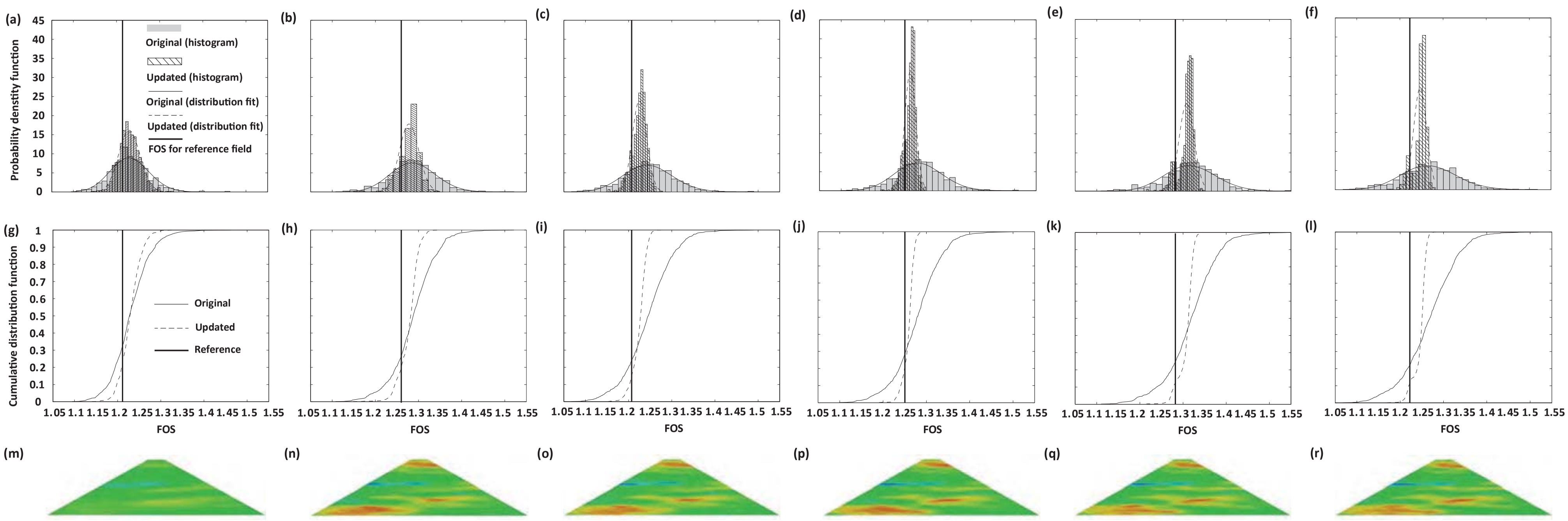

Figure 9 Improved prediction of the distribution of FOS: (a) - (f) PDF before 2nd, 4th, 6th, 8th, 10th and 12th assimilation stps; (g) - (l) CDF before 2nd, 4th, 6th, 8th, 10th and 12th assimilation steps; (m) - (r) Updated lnk_{sat} field after 1st, 3rd, 5th, 7th, 9th and 11th assimilation steps.

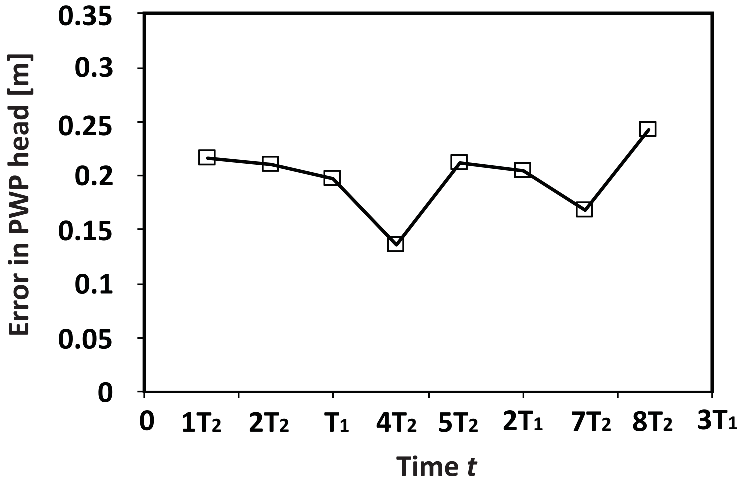

Figure 10 Error in PWP versus time.

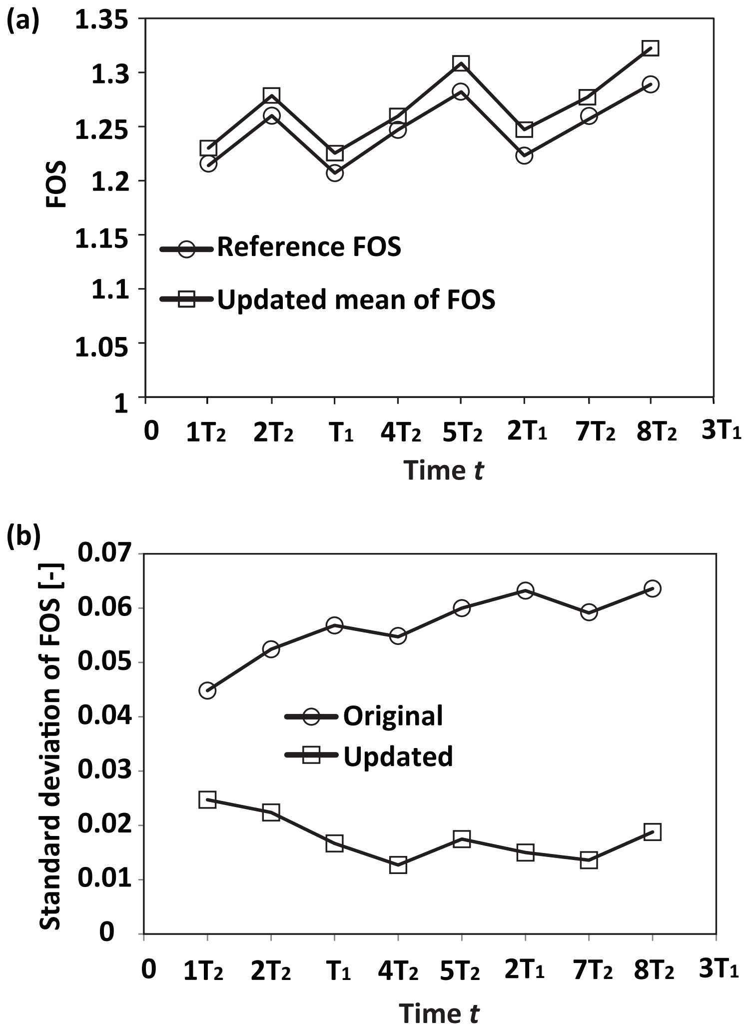

Figure 11 (a) FOS and (b) standard deviation of FOS versus time for the original and updated ensembles.

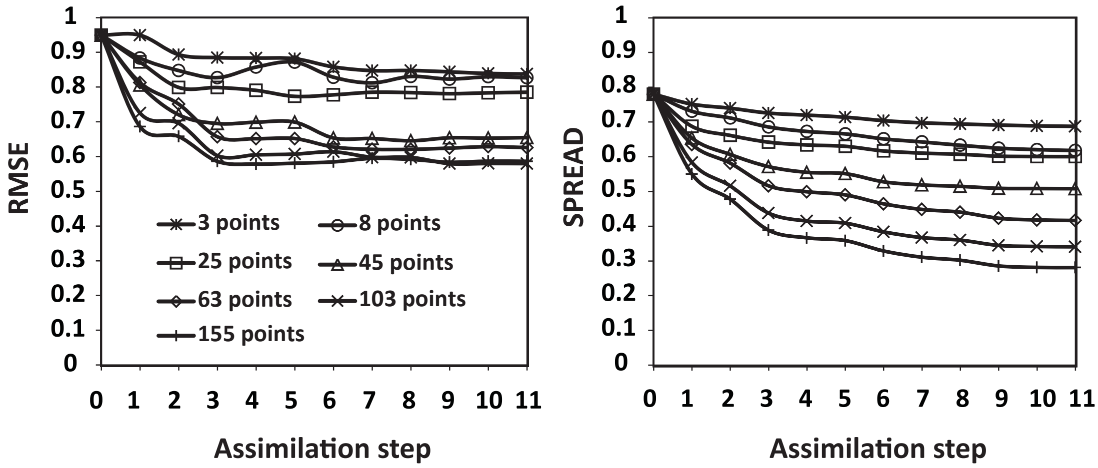

Figure 12 Sensitivity of RMSE and SPREAD to the number of measurement points.

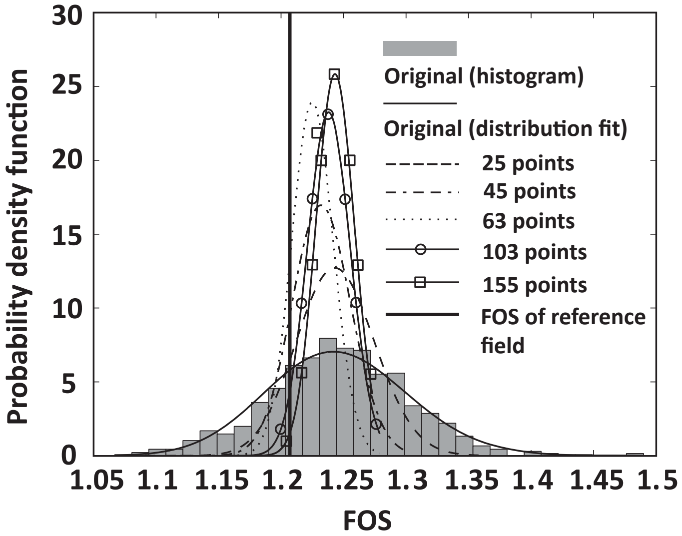

Figure 13 Influence of the number of measurement points on the distribution of FOS.

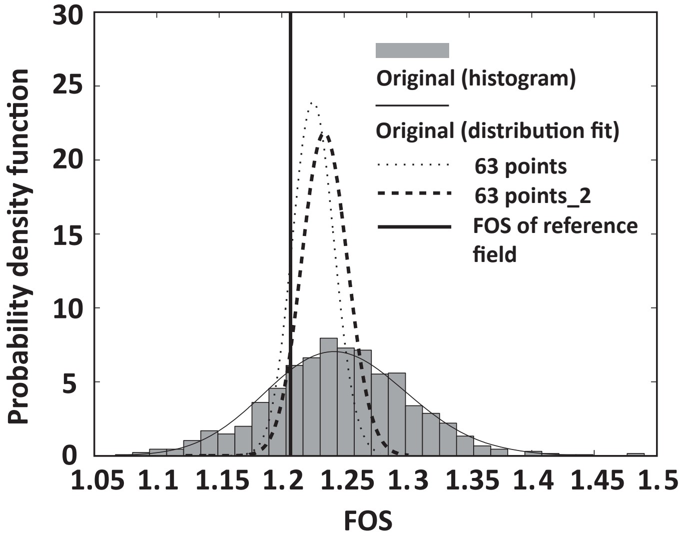

Figure 14 Comparison of FOS distributions for two different configurations of 63 measurement points.

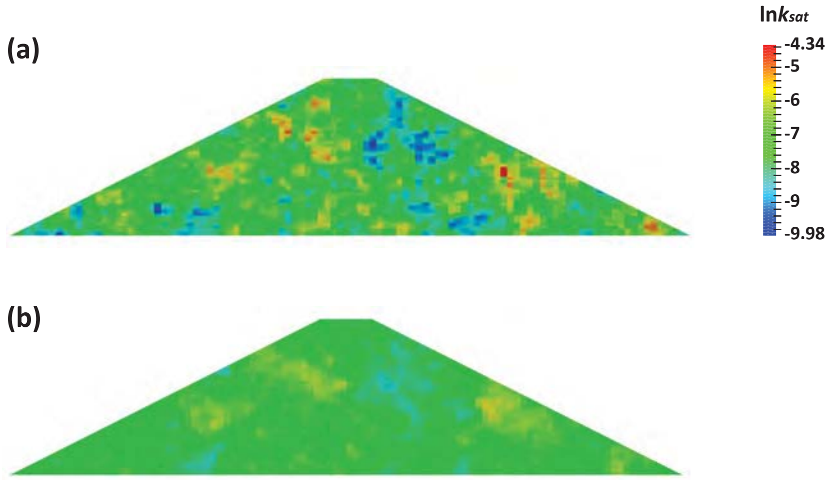

Figure 15 Improved estimation of lnk_{sat} field (l_v = l_h = 2 m): (a) Reference field; (b) Improved estimation after 11th assimilation step based on 63 measurement points.

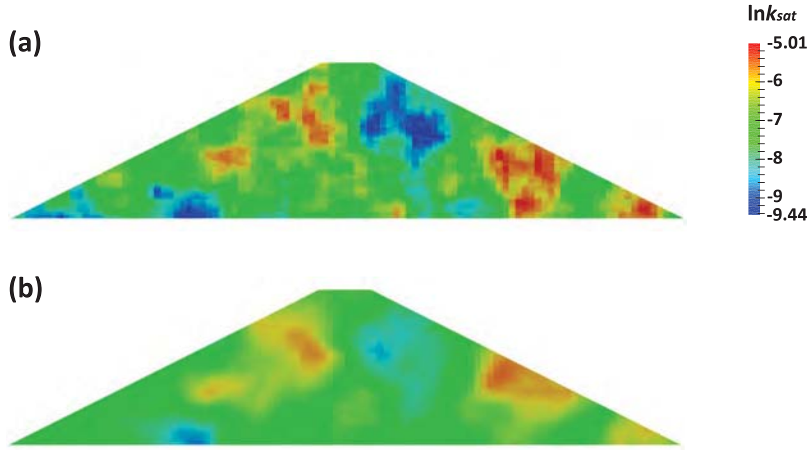

Figure 16 Improved estimation of lnk_{sat} field (l_v = l_h = 8 m): (a) Reference field; (b) Improved estimation after 11th assimilation step based on 63 measurement points.

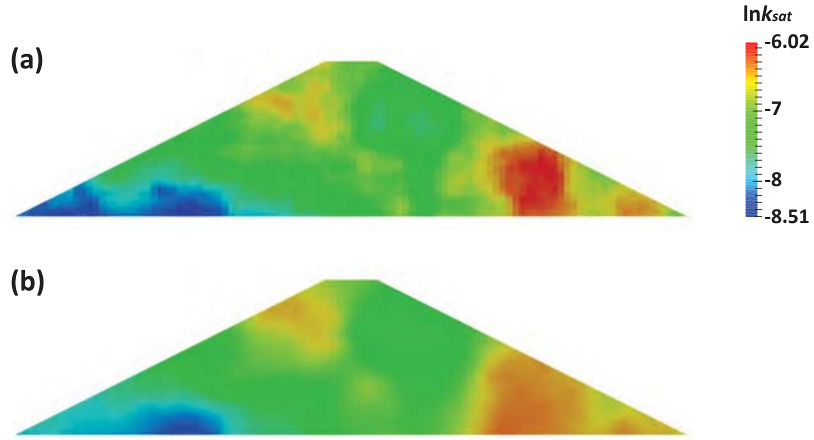

Figure 17 Improved estimation of lnk_{sat} field (l_v = l_h = 64 m): (a) Reference field; (b) Improved estimation after 11th assimilation step based on 63 measurement points.

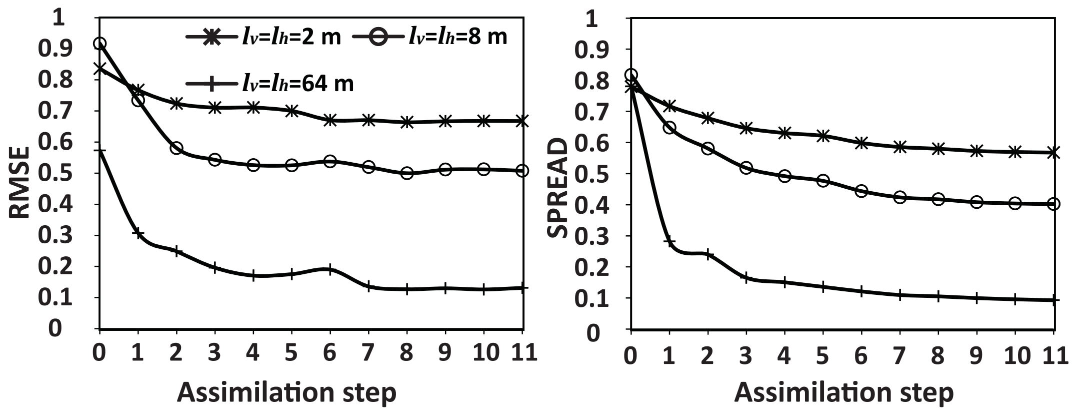

Figure 18 Variation of RMSE and SPREAD with SOF for isotropic random fields.

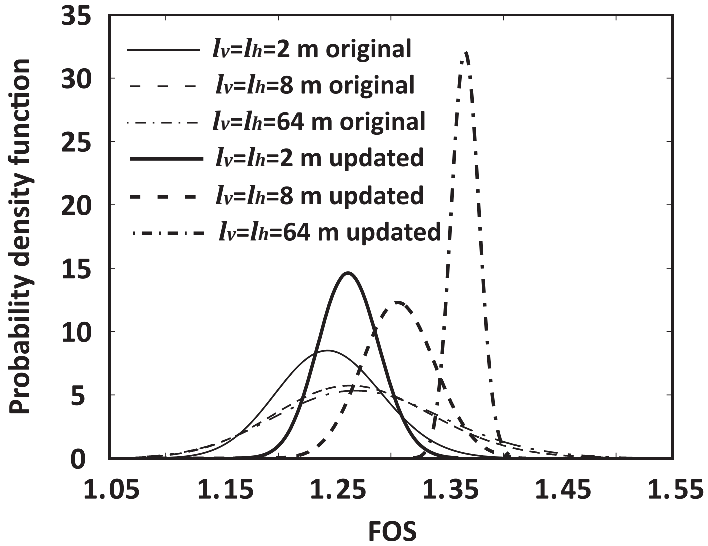

Figure 19 Comparison between the original and updated distributions of FOS for different l.

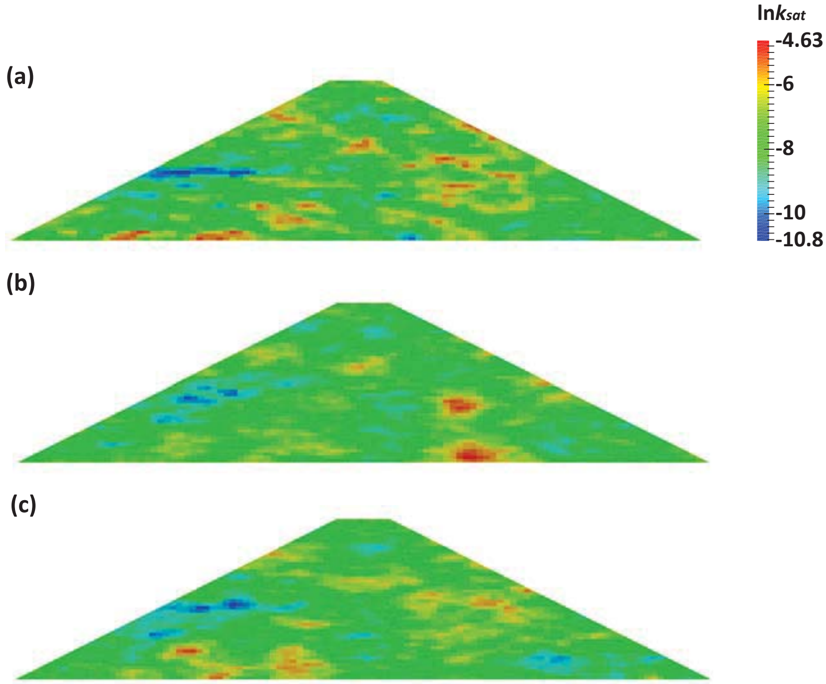

Figure 20 Improved estimation of lnk_{sat} field (l_v = 1 m and l_h = 2 m): (a) Reference field; (b) Improved estimation after 11th assimilation step based on 63 measurement points; (c) Improved estimation after 11th assimilation step based on 103 measurement points.

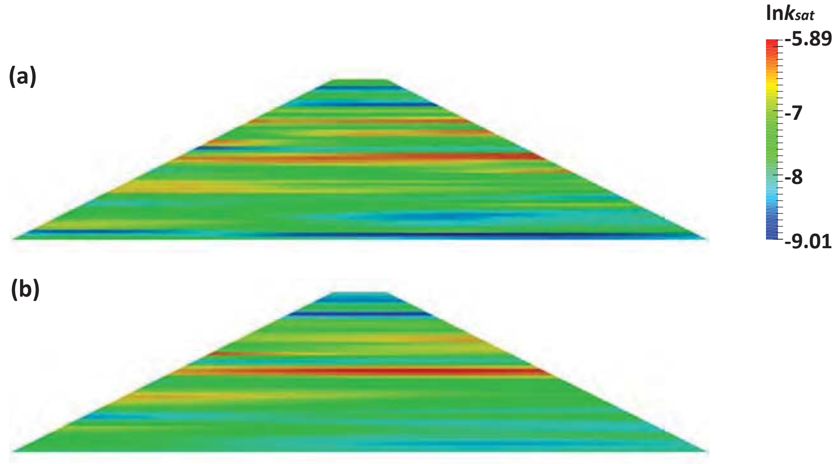

Figure 21 Improved estimation of lnk_{sat} field (l_v = 1 m and l_h = 64 m): (a) Reference field; (b) Improved estimation after 11th assimilation step based on 63 measurement points.

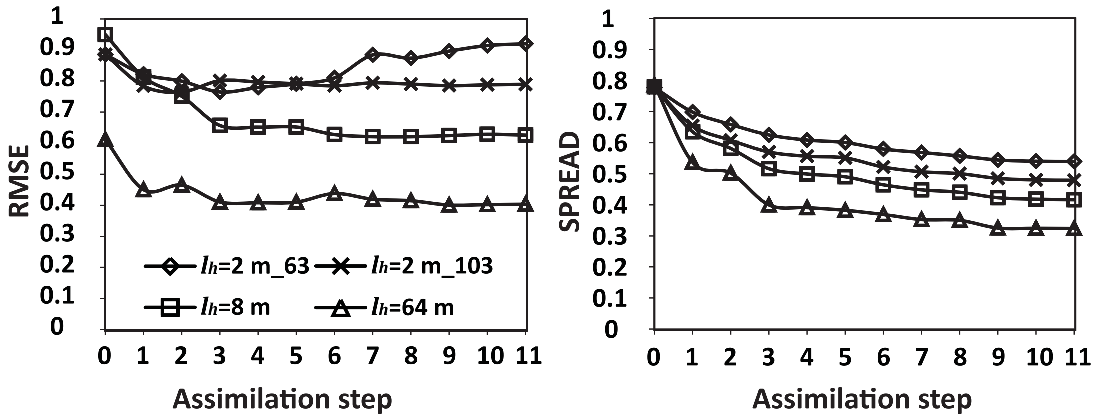

Figure 22 Variation of RMSE and SPREAD with SOF for anisotropic random fields.

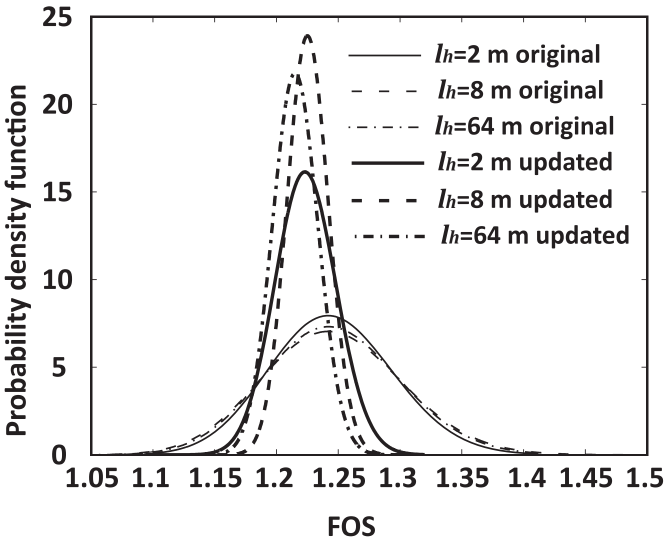

Figure 23 Comparison between the original and updated distributions of FOS for different l_h (l_v = 1 m).

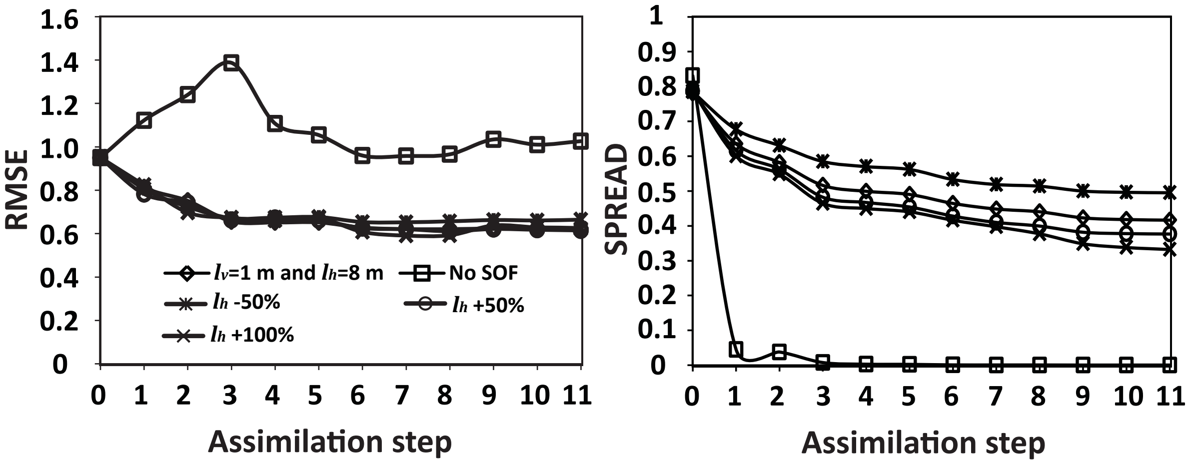

Figure 24 Influence of inaccuracy in l_h on variation of RMSE and SPREAD.

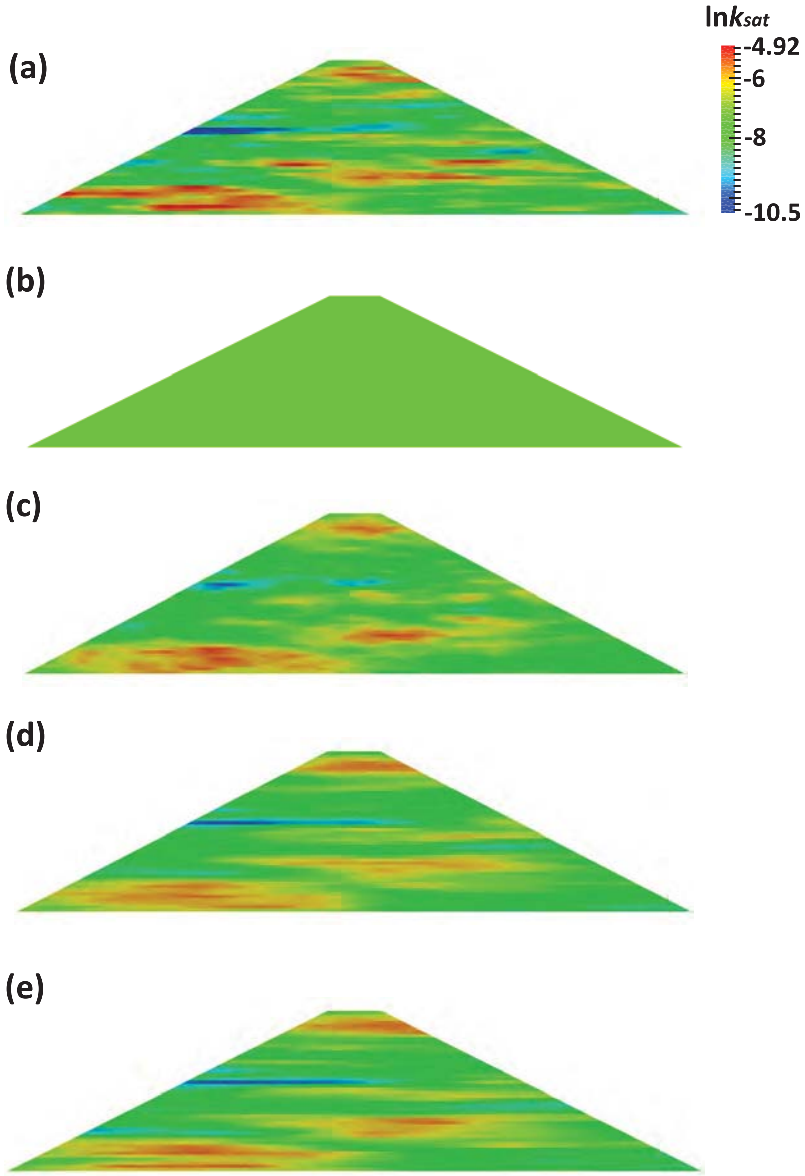

Figure 25 Improved estimation of lnk_{sat} field based on 63 measurement points and various estimates for l_h relative to l_h = 8 m: (a) Reference field; (b) Improved estimation (no SOF); (c) Improved estimation (l_h -50%); (d) Improved estimation (l_h +50%); (e) Improved estimation (l_h +100%).

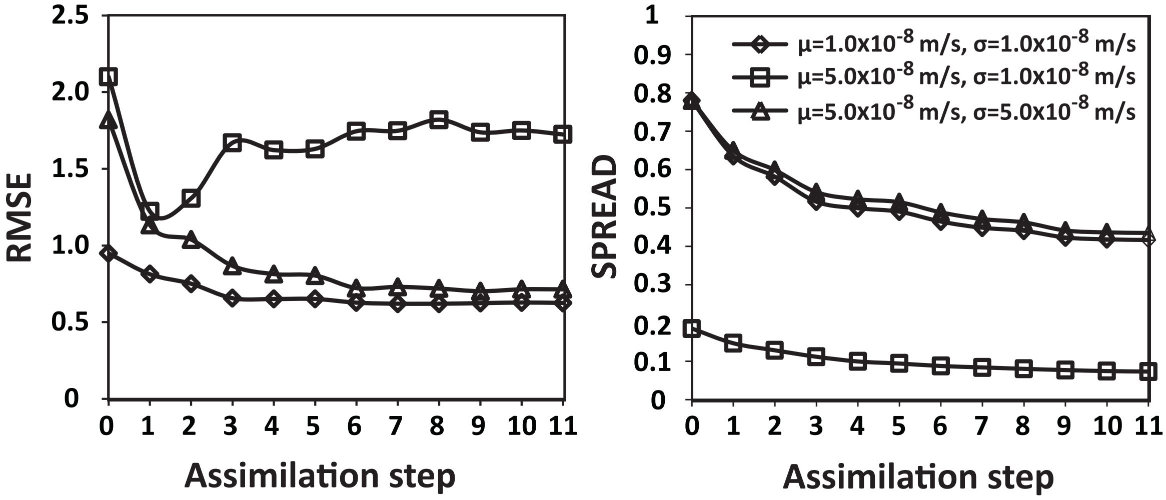

Figure 26 Variation of RMSE and SPREAD for cases with accurate and inaccurate initial conditions.

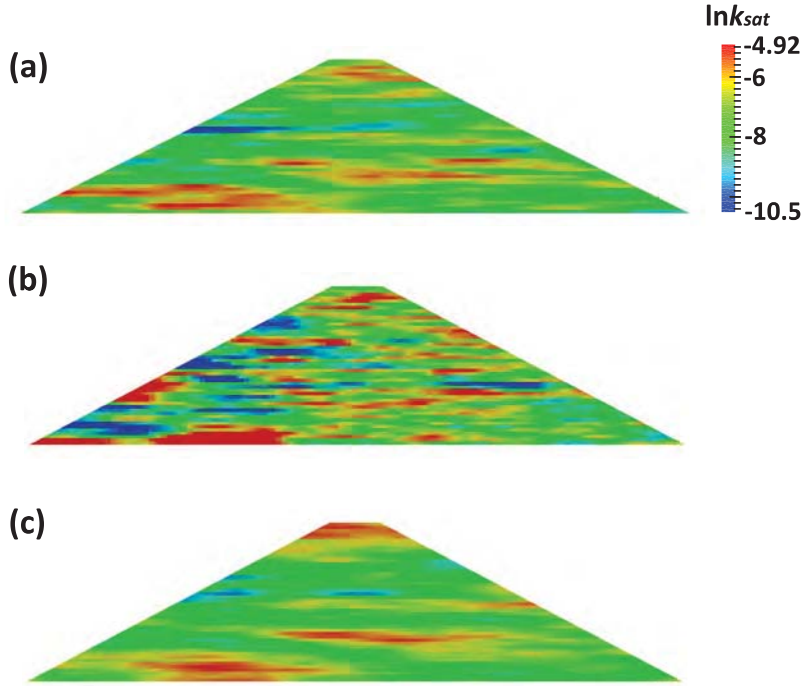

Figure 27 Improved estimation of lnk_{sat} field with inaccurate initial conditions: (a) Reference field; (b) Improved estimation after 11th assimilation step with inaccurate mean only; (c) Improved estimation after 11th assimilation step with both inaccurate mean and standard deviation.

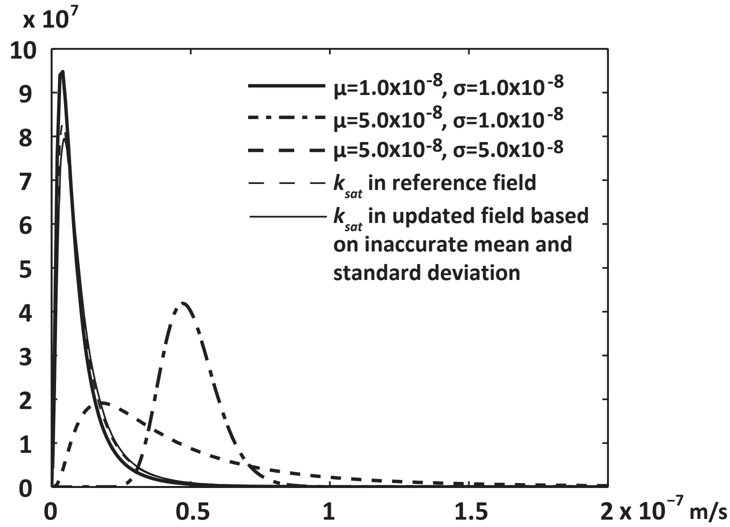

Figure 28 Distributions of k_{sat} for different means and standard deviations.

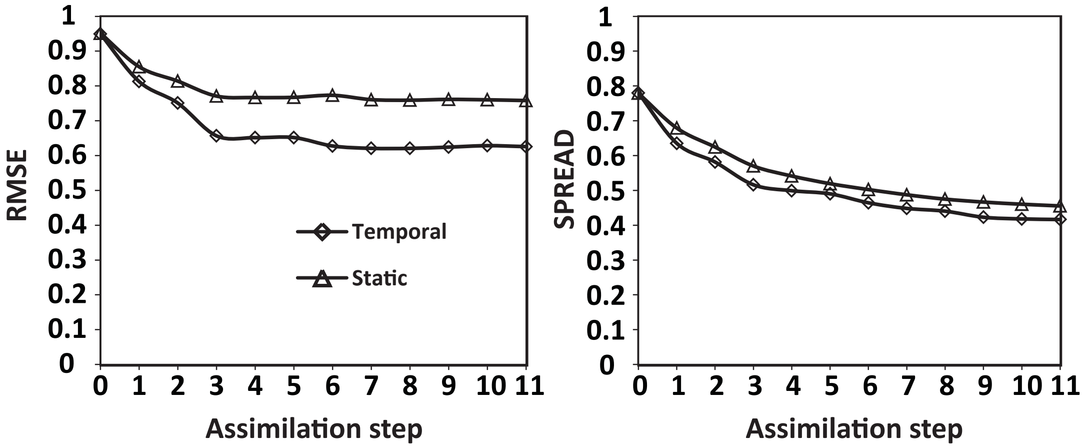

Figure 29 RMSE and SPREAD for static and temporal measurements.

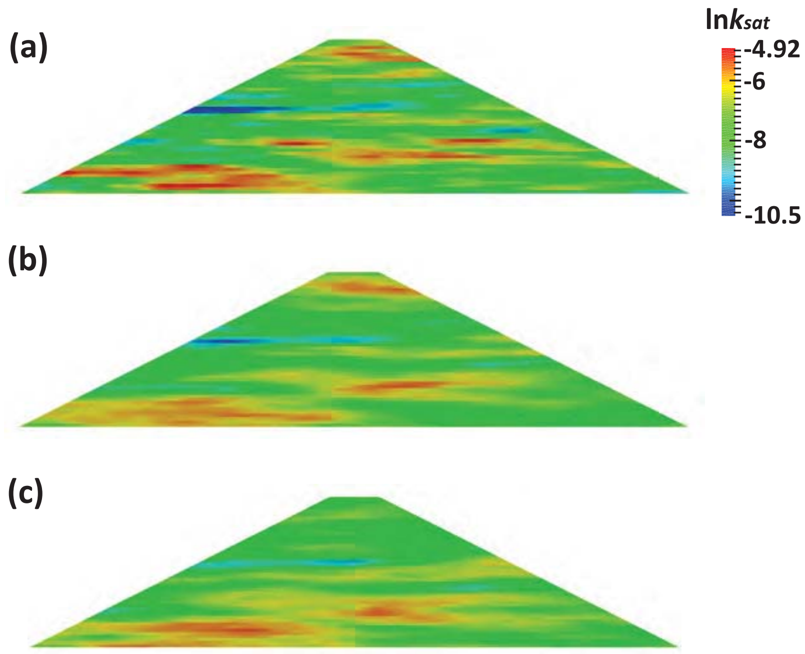

Figure 30 Improved estimation of lnk_{sat} field: (a) Reference field; (b) Improved estimation after 11th assimilation step using temporal measurements; (c) Improved estimation after 11th assimilation step using static measurements.

Table 1 Parameter values for the illustrative example.

Parameter	Symbol	Unit	Value
VGM parameter for the curve	α_d	m^{-1}	0.1
Fitting parameter for VGM model	n	-	1.226
Saturated volumetric water content	θ_s	-	0.38
Residual volumetric water content	θ_r	-	0.0038
Stiffness	E	kPa	1.0×10^5
Poisson's ratio	υ	-	0.3
Effective cohesion	c'	kPa	15
Effective friction angle	φ'	^{o}	20
Dilation angle	ψ	^{o}	0
Specific unit weight	G_s	-	2.02

Note: VGM denotes the Van Genuchten–Mualem model.

Table 2 Scenarios of different numbers of measurement points.

Scenario	Columns selected	Number of measurement points
1	±12, ±10, ±8, ±6, ±4, ±2, 0	155
2	±12, ±9, ±6, ±3, 0	103
3	±10, ±5, 0	63
4	±7, 0	45
5	±12, 0	25
6	Points in ±10, ±5, 0 ('—')	8
7	Points in ±5, 0 ('/')	3

Note: ± indicates both positive and negative column numbers; the symbols '—' and '/' indicate the positions of the points in scenarios 6 and 7, respectively.

Table 3 Inaccurate mean and standard deviation of k_{sat} used in the EnKF.

Case		Mean (m/s)	Standard deviation (m/s)	l_v (m)	l_h (m)
Accurate		1.0×10^{-8}	1.0×10^{-8}		
Inaccurate	1	5.0×10^{-8}	1.0×10^{-8}	1	8
	2	5.0×10^{-8}	5.0×10^{-8}		